

# Spatial Properties of Industrial Wireless Ultra-Reliable Low-Latency Communication MIMO Links

Stefan Zelenbaba<sup>1</sup>, Markus Hofer<sup>1</sup>, David L öschenbrand<sup>1</sup>, Georg Kail<sup>2</sup>, Martin Schiefer<sup>2</sup>, Thomas Zemen<sup>1</sup>

<sup>1</sup>*Center for Digital Safety & Security, Austrian Institute of Technology GmbH, Vienna, Austria*

<sup>2</sup>*CT REE ELM RFT-AT, Siemens AG Österreich, Vienna, Austria*

stefan.zelenbaba@ait.ac.at

**Abstract**—We show the results of a measurement campaign done in an industrial hall, and analyse a frequency-selective  $2 \times 2$  multiple-input multiple-output channel. The transmitter is kept static while the receiver moves across a positioning board between line-of-sight and obstructed line-of-sight. We compare capacities, delay spreads and fading patterns of different antenna settings. We observe that higher outage capacity is achieved when using co-polarized rather than cross-polarized dipoles. The settings with higher capacity rates also show lower root-mean-square delay spread values, due to the presence of a strong line-of-sight component. We observe how polarization and antenna alignment influence the fading patterns.

keywords: 5G, wireless, MIMO, industrial URLLC

## I. INTRODUCTION

5G ultra-reliable low-latency wireless communication (URLLC) links are an important component for wireless automation and control systems in future production environments. Nevertheless, due to complex structures and reflective materials commonly found in industrial environments, an abundance of multi-path components (MPCs) can be expected, which makes the task of designing URLLC systems challenging. An important step towards understanding and exploiting the propagation effects in such cases is collecting on-site empirical data and evaluating key statistical metrics that can then be used to develop a suitable channel model.

A channel sounding campaign with a signal bandwidth of 100 MHz is done in [1], where the authors observe an exponentially decaying power delay profile (PDP) with maximum excess delay of  $\approx 500$  ns. A similar trend is observed in [2] where delay spreads for line-of-sight (LoS) and non-LoS (NLoS) are analyzed. However, the measurements performed are single-input-single-output (SISO).

In this paper, a software-defined radio (SDR) based channel sounder is used to capture the characteristics of a  $2 \times 2$  multiple-input-multiple-output (MIMO) wireless link, set in an industrial hall. The collected data is then used to analyze fading patterns, and derive

frequency-dependent channel capacity values and root-mean-square (RMS) delay spreads.

## Contributions of the Paper:

- We analyze the characteristics of wireless, frequency-selective  $2 \times 2$  MIMO channels in an industrial environment.
- We compare different antenna settings in terms of capacity and RMS delay spread, and observe the changes in the fading patterns.

## Notation:

We denote a scalar by  $a$ , a column vector by  $\mathbf{a}$  and its  $i$ -th element with  $a_i$ . Similarly, we denote a matrix by  $\mathbf{A}$  and its  $(i, \ell)$ -th element by  $a_{i,\ell}$ . The conjugate transpose of  $\mathbf{A}$  is given by  $\mathbf{A}^H$ . The  $Q \times Q$  identity matrix is denoted by  $\mathbf{I}_Q$ . We define the Frobenius norm of a matrix as  $\|\mathbf{A}\|_F$ . The absolute value of  $a$  is denoted by  $|a|$ . We denote the set of all complex numbers by  $\mathbb{C}$ . We define the notation  $\mathbf{a} = \text{vec}(\mathbf{A}) = \text{vec}((a_{i,\ell})) \in \mathbb{C}^{MN \times 1}$ , where  $\text{vec}(\mathbf{A})$  denotes the vectorized version of matrix  $\mathbf{A}$ , formed by stacking the columns of  $\mathbf{A}$  into a single column vector.

## II. MIMO CHANNEL CHARACTERISATION

We want to observe the behavior of different antenna settings and compare them in terms of outage capacity. We also want to obtain statistical data and metrics that can be used to model the channel. The receiver (Rx) antenna is moving across the two-dimensional positioning table, hence the channel properties are changing with its position. Therefore, an indexing notation alternative to time is chosen, namely position indexes  $x \in \{1, \dots, X\}$ , and  $y \in \{1, \dots, Y\}$ . Each position pair  $(x, y)$  consists of  $M$  channel snapshots. For simplicity, we use  $k \in \{1, \dots, K\}$ , where  $K = XY$ , to describe each position pair  $(x, y)$ . We define  $M$  as the length of the stationarity region, for which we assume the channel to be stationary. Therefore, we describe the MIMO wireless channel

using the channel matrix  $\mathbf{G}[m, q; k] \in \mathbb{C}^{M_{\text{T}} \times M_{\text{R}}}$ , and its vectorized version  $\mathbf{g}[m, q; k] = \text{vec}(\mathbf{G}[m, q; k])$ , where  $q \in \{1, \dots, Q\}$  denotes the frequency (subcarrier) index and  $m \in \{1, \dots, M\}$  denotes the stationarity region snapshot index. The channel matrix entries are frequency dependent channel transfer functions  $g_{i,j}[m, q; k]$ , between transmit antenna  $i$  and receive antenna  $j$ .

The Frobenius norm of the frequency-selective MIMO channel over all subcarriers is used to describe the fading patterns, as it represents the total energy of the MIMO channel [3]. It is calculated as

$$\|\mathbf{g}\|_{\text{F}}^2[k] = \frac{1}{QM} \sum_{m=1}^M \sum_{q=1}^Q \sum_{i=1}^{M_{\text{T}}} \sum_{j=1}^{M_{\text{R}}} |g_{i,j}[m, q; k]|^2. \quad (1)$$

*Capacity:* The channel information is unknown at the transmitter (Tx), so no power allocation schemes such as water-filling are used. Instead we assume the transmit power to be equally distributed over both Tx antennas. The space-variant MIMO channel capacity for frequency-selective channels can be computed as in [4]:

$$C[k] = \frac{1}{\hat{Q}M} \sum_{m=1}^M \sum_{q=Q/2-\hat{Q}/2}^{Q/2+\hat{Q}/2} \log_2 \det \left( \mathbf{I}_{M_{\text{R}}} + \frac{\rho}{M_{\text{T}}} \mathbf{G}^{\text{H}}[m, q; k] \mathbf{G}[m, q; k] \right), \quad (2)$$

where  $\rho = P_{\text{t}}/N_0$  presents the average SNR at the Rx side, with  $P_{\text{t}}$  being the total transmit power and  $N_0$  the noise floor level. This formula is derived from a more general one, presented in [5]. It is important to average only over the bandwidth that corresponds to the analyzed system. Averaging over a larger bandwidth increases the steepness of the capacity cumulative distribution function (CDF) curve [4] and leads to inaccurate calculations of outage capacity values. Thus, we take  $\hat{Q}$  subcarriers from the middle of the total signal bandwidth. For each region in space the capacity is then averaged over its  $M$  snapshots.

*LSF:* We can describe the Doppler-delay statistics of the channel by calculating the local scattering function (LSF) [6] for every stationarity region  $k$  of every MIMO channel. The LSF is a multi-taper estimate [7] of the scattering function, obtained as:

$$\hat{P}_{\tau, \nu; i, j}[k; n, p] = \frac{1}{I_1 I_2} \sum_{w=1}^{I_1 I_2} |\mathcal{G}_{i,j}^{(G_w)}[k; n, p]|^2, \quad (3)$$

where  $n \in \{1, \dots, Q\}$  is the delay bin index. The windowed frequency transfer function  $\mathcal{G}_{i,j}^{(G_w)}$  is calculated

as

$$\mathcal{G}_{i,j}^{(G_w)}[k; n, p] = \sum_{m'=-M/2}^{M/2-1} \sum_{q'=-Q/2}^{Q/2-1} g_{i,j}[m' - k, q' - k] G_w[m', q'] e^{-j2\pi(pm' - nq')}. \quad (4)$$

The Doppler shift is indexed by  $p \in \{-M/2, \dots, M/2 - 1\}$ . The window function

$$G_w[m', q'] = u_{i_1}[m' + M/2] \tilde{u}_{i_2}[q' + N/2], \quad (5)$$

is constructed using band-limited discrete prolate spheroidal sequences (DPSS) [8]  $u_{i_1}$ , indexed with  $i_1 \in \{1, \dots, I_1\}$ , and  $u_{i_2}$ , indexed with  $i_2 \in \{1, \dots, I_2\}$ , while  $w = i_1 I_2 + i_2$ . Integrating over the LSF in the Doppler domain gives us the space-variant PDP as

$$\hat{P}_{\tau; i, j}[k; n] = \frac{1}{M} \sum_{p=-M/2}^{M/2-1} \hat{P}_{\tau, \nu; i, j}[k; n, p]. \quad (6)$$

An important parameter that influences the design of OFDM systems in scatterer-rich environments is the delay spread, which can be interpreted as the multipath richness of the channel. We obtain the RMS delay spread as [9]

$$\sigma_{\tau; i, j}[k] = \sqrt{\frac{\sum_{n=1}^N (n\tau_s)^2 \hat{P}_{\tau; i, j}[k; n]}{\sum_{n=1}^N \hat{P}_{\tau; i, j}[k; n]} - \bar{\tau}_{i, j}[k]^2}, \quad (7)$$

where

$$\bar{\tau}_{i, j}[k] = \frac{\sum_{n=1}^N (n\tau_s) \hat{P}_{\tau; i, j}[k; n]}{\sum_{n=1}^N \hat{P}_{\tau; i, j}[k; n]}, \quad (8)$$

and  $\tau_s$  is the resolution in the delay domain. In calculating the RMS delay spread, we apply two power thresholds according to the power threshold criterion [10]. We set the noise floor threshold, to disregard spurious noise components that might be mistaken for MPCs, and the sensitivity threshold that disregards any components that are too weak to be taken into account. We then only consider delay indexes that have higher power than both of them (see Fig. 5).

### III. CHANNEL SOUNDER IMPLEMENTATION

The main component of each channel sounder node is an SDR universal software radio peripheral (USRP), which is controlled and configured by a host computer. Sounding interval synchronization and triggering is done using a common pulse-per-second (PPS) signal, provided by GPS disciplined rubidium oscillators. On the Tx side, the signal is amplified with an external, 27 dB power amplifier. We use the switched-array principle for MIMO operation, i.e. a different

transmit-receive antenna combination is active during each sounding interval as shown in Fig. 1. For this purpose, TTL logic PIN-diode switches are used on both sides.

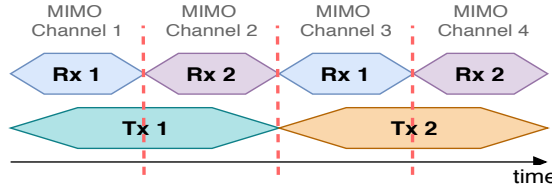


Fig. 1. Antenna switching pattern of a single MIMO snapshot

### A. Sounding Principle

A complex baseband multi-tone (OFDM based) sounding sequence, with sampling rate  $1/T_S$  is transmitted in equidistant bursts (snapshots). The sequence consists of  $Q$  subcarriers, spaced by  $\Delta f = 1/T$ , thus the total signal bandwidth is  $B = Q\Delta f$ . Each sequence consists of three identical copies of the sounding signal, followed by a silent period. The first half of the first signal copy is used as a cyclic prefix and the last half of the last copy as a guard period. The middle part (two copies of the signal) is used to obtain the oversampled spectrum of the received signal, as shown in Fig. 2. The silent period allows time for antenna switching, buffer emptying and data recording. The sounding signal itself is designed so that it has a low crest factor [11] over its duration  $T$ . This is achieved by optimizing the subcarrier phases with the algorithm proposed in [12].

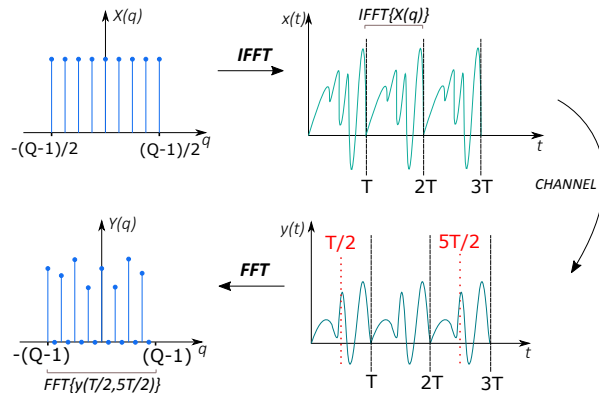


Fig. 2. Sounding signal structure. Two signal copies are cut out from the middle of the transmitted sounding sequence at the Rx side. The spectrum is then obtained via oversampled FFT.

The  $q$ -th subcarrier of the received signal between transmit antenna  $i$  and receive antenna  $j$  can be written as  $Y_{i,j}[q] = X[q]G_{i,j}^{\text{RF}}[q]G_{i,j}[q]$  where  $X[q]$  is the known transmitted signal and  $G_{i,j}[q]$  is the wireless channel transfer function. The radio frequency (RF) chain transfer function  $G_{i,j}^{\text{RF}}[q]$  is introduced by the hardware components. In order to obtain it, we measure

the transfer function of each MIMO channel via a direct cable connection between the corresponding Tx and Rx antenna ports. It is then used to calculate the calibrated channel transfer functions as  $G_{i,j}[q] = Y_{i,j}[q]/X[q]G_{i,j}^{\text{RF}}[q]$ .

### IV. MEASUREMENT CAMPAIGN

1) *Sounding Parameters:* We use  $M_T = 2$  Tx and  $M_R = 2$  Rx antennas. The carrier frequency of  $f_c = 3.5$  GHz is chosen for its planned use in 5G applications. The used multi-tone signal consists of  $Q = 601$  subcarriers, spaced  $\Delta f = 250$  kHz, which gives the total signal bandwidth of  $B = 150$  MHz. The signal is optimized so it has a crest factor of 1.25. The sounding signal is  $T = 4.26 \mu\text{s}$  long, hence the whole sounding sequence is  $3T = 12.8 \mu\text{s}$ . The interval between single snapshots is set to  $T_{\text{snapshot}} = 500 \mu\text{s}$ . Therefore, the total length of one full MIMO snapshot is  $M_R M_T T_{\text{snapshot}} = 2$  ms. The summary of chosen measurement parameters is given in Tab. I.

TABLE I  
MEASUREMENT PARAMETERS

Parameter	Value
Antenna configuration	$2 \times 2$ MIMO
Carrier frequency	3.5 GHz
Measurement bandwidth	150 MHz
MIMO snapshot rate	2 ms

2) *Campaign Setup:* The measurement campaign was carried out in a Siemens factory hall in Vienna, Austria, with plenty of complex metallic structures surrounding the measurement setup and covering the ceiling. The layout of the setup and its environment is shown in Fig. 3. The Tx antenna is kept static at all times, while the Rx antenna is moving across the  $2 \text{ m} \times 1 \text{ m}$  wooden positioning board. Both antennas are mounted at a height of  $h = 1.25$  m. The Rx antenna is moving across the shorter side of the board (Y-axis), with a maximum velocity of  $v = 1 \text{ m/s}$ . With each run, the Rx antenna shifts closer to the Tx by one half of the carrier frequency wavelength  $\lambda/2 = 4.25 \text{ cm}$ , on the X-axis. Each run is repeated  $X = 44$  times before the Rx antenna reaches the positioning plate end, i.e. the Rx antenna moves  $22\lambda$  across the X-axis, during one measurement. The effective area of the Rx antenna movement is thus 92 cm on the Y-axis and 187 cm on the X-axis. A metallic reflecting plate is placed half-way between the nodes, thus creating NLoS conditions for a part of the Rx trajectory.

3) *Antennas:* We use dual-polarized cross-dipole antennas depicted in Fig. 4, with 5 dBi gain each. The alignment and the active dipole combinations are changed and compared in terms of aforementioned performance metrics. Afterwards, the geometry and the Tx antenna position are changed to create additional scenarios. Tab. II lists the settings of all measurement scenarios together with the reference Scenario 0, where

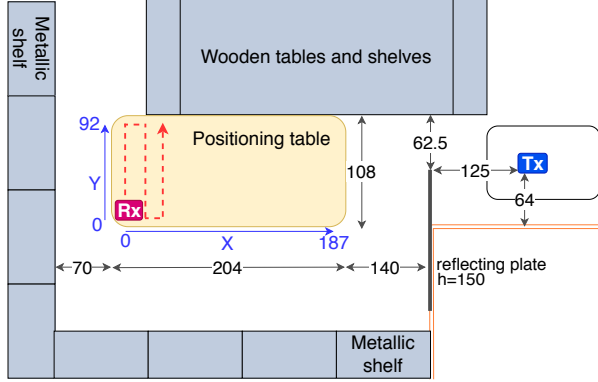


Fig. 3. Aerial view diagram of the factory hall and measurement equipment layout. Distances are given in cm. The red-dashed line depicts the Rx antenna trajectory

the reflecting plate is not present. In each scenario both nodes always use the same antenna configuration and alignment.

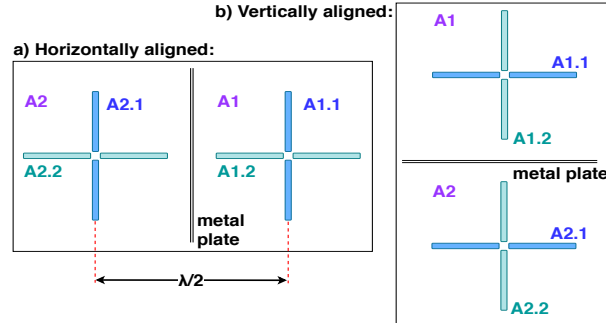


Fig. 4. Front view diagram of the used antennas. Each antenna set consists of two cross-dipole antennas, A1 and A2, separated by a metallic plate and spaced  $\lambda/2$ . The antenna structure can be either horizontally (a) or vertically (b) aligned. Two of four dipoles are always active on each side of the link.

TABLE II  
MEASUREMENT SCENARIOS

	Scenario	Alignment	Active dipoles
0	No reflecting plate	Vertical	A1.1+A2.2
1	with reflecting sheet	Horizontal	A1.1+A2.1
2	with reflecting sheet	Horizontal	A1.1+A2.2
3	with reflecting sheet	Horizontal	A1.2+A2.2
4	with reflecting sheet	Horizontal	A1.2+A1.1
5	with reflecting sheet	Vertical	A1.1+A2.1
6	with reflecting sheet	Vertical	A1.1+A2.2
7	with reflecting sheet	Vertical	A1.2+A2.2
8	Tx on double distance	Vertical	A1.1+A2.2
9	Tx on triple distance	Vertical	A1.2+A2.2
10	Constant NLoS	Vertical	A1.1+A2.2
11	Added reflecting sheets	Vertical	A1.1+A2.2
12	Tx elevated at $h = 3.5$ m	Vertical	A1.1+A2.2

4) *Metric Evaluation:* For metric evaluation we choose the stationarity region of  $M = 42$  MIMO snapshots, as it corresponds to the Rx antenna moving by almost one full wavelength at  $v = 1\text{ m/s}$ . This corresponds to  $T_{\text{stat}} = MT_{\text{snapshot}} = 84\text{ ms}$  in time,

and  $Y = 15$  evaluations in each run. In calculating the RMS delay spread, the noise threshold of 15 dB above the noise floor is chosen together with the sensitivity threshold of 35 dB below the strongest component.

## V. RESULTS

1) *PDP:* An exponentially decaying PDP is observed in the measurements, as it has been shown in [1] and [2]. The maximum excess delay ranges between 400 ns and 600 ns, as presented in Fig. 5.

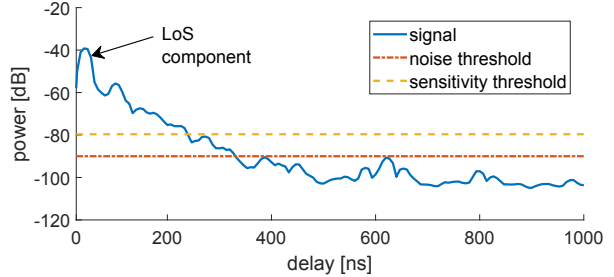


Fig. 5. PDP of a single MIMO channel showing a typical delay spread in the measurement environment.

2) *Capacity:* The system bandwidth is  $\hat{B} = 20\text{ MHz}$ , so to obtain capacity we sum over  $\hat{Q} = 81$  subcarriers. All measurements are normalized with the average path-loss value obtained for Scenario 0. An SNR value of  $\rho = 20\text{ dB}$  is used in the calculations. The capacity CDFs of different antenna configurations are shown in Fig. 6. As our focus is on the reliability aspect, we look at the outage capacity values. The co-polarized dipole pairs perform better due to the higher average SNR between the antenna pairs, as there is no cross-polar discrimination (XPD). Settings with vertically aligned antennas show better performance. In Scenario 4 the dipoles are not spatially separated and this yields the worst performance.

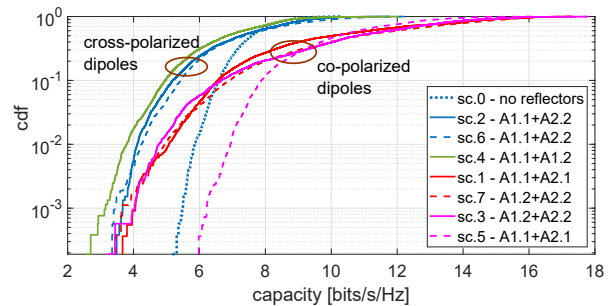


Fig. 6. Capacity CDFs for different antenna settings. The dashed lines present vertically aligned configurations while the full lines present horizontally aligned ones. The dotted line presents Scenario 0, with no reflecting plate to introduce NLoS conditions.

Fig. 7 shows the capacity CDFs of additional scenarios together with one of the standard settings with the reflecting plate. When the Tx is placed behind a corner (constantly in NLoS) performance drops, while the setting with added reflective sheets gives the highest capacity.

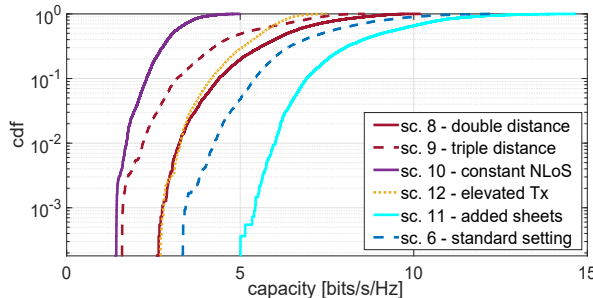


Fig. 7. Capacity CDFs for different scenarios. All the scenarios use the same antenna settings

3) *RMS delay spread*: In Fig. 8 we see that scenarios that showed higher capacity values show lower RMS delay spread. Since they have a strong LoS component over all the channels the RMS delay spread value is smaller.

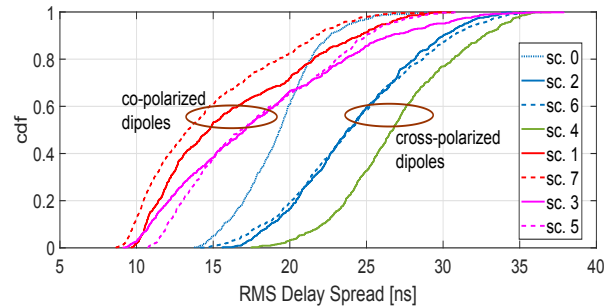


Fig. 8. CDFs of RMS delay spreads for different antenna settings.

4) *Fading patterns*: Fig. 9 shows the fading patterns obtained from (1), for Scenarios 1, 3 and 7. Upon changing the polarization of the dipoles from vertical to horizontal, we observe a two-path fading pattern. The fading dips occur at roughly every  $8\lambda$  as the Rx moves down the X-axis. The pattern difference is likely caused by polarization-dependent diffraction coefficients. We see that changing the antenna alignment (in Scenario 7) also has an impact on the fading pattern.

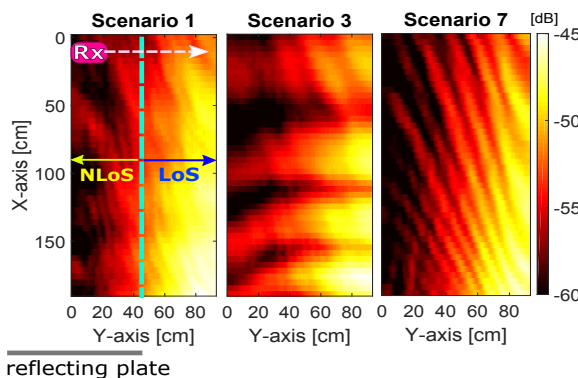


Fig. 9. Fading patterns over the positioning table for Scenario 1 (horizontal polarization and alignment), Scenario 3 (vertical polarization, horizontal alignment) and Scenario 7 (horizontal polarization, vertical alignment). For better resolution, the stationarity region of length  $M = 5$  is used.

## VI. CONCLUSIONS

In this paper we analyze the properties of a frequency-selective  $2 \times 2$  MIMO channel in an industrial environment, and compare different antenna settings. We observe that using co-polarized antennas yields higher outage capacity values. Aligning the antenna array vertically rather than horizontally also improves capacity values. Changing dipole polarization and antenna alignment impacts the fading patterns. The maximum excess delay is shown to vary between 400 ns and 600 ns. Based on the obtained data we will develop a stochastic industrial channel model, with an exponentially decaying PDP and the LoS component in the first delay tap.

## VII. ACKNOWLEDGMENTS

This work is funded by the Austrian Research Promotion Agency (FFG) and the Austrian Ministry for Transport, Innovation and Technology (bmvit) within the project UNWIRE (858675) of the funding program Production of the Future.

## REFERENCES

- [1] E. Tanghe, D. P. Gaillot, M. Linard, L. Martens, and W. Joseph, "Experimental analysis of dense multipath components in an industrial environment," *IEEE Transactions on Antennas and Propagation*, vol. 62, no. 7, pp. 3797–3805, July 2014.
- [2] B. Hofeld, D. Wieruch, L. Raschkowski, T. Wirth, C. Pallasch, W. Herfs, and C. Brecher, "Radio channel characterization at 5.85 ghz for wireless m2m communication of industrial robots," in *2016 IEEE Wireless Communications and Networking Conference*, April 2016, pp. 1–7.
- [3] C. Oestges and B. Clerckx, *MIMO Wireless Communications: From Real-World Propagation to Space-Time Code Design*. Orlando, FL, USA: Academic Press, Inc., 2007.
- [4] A. F. Molisch, M. Steinbauer, M. Toeltsch, E. Bonek, and R. S. Thoma, "Capacity of mimo systems based on measured wireless channels," *IEEE Journal on Selected Areas in Communications*, vol. 20, no. 3, pp. 561–569, April 2002.
- [5] G. Foschini and M. Gans, "On limits of wireless communications in a fading environment when using multiple antennas," *Wireless Personal Communications*, vol. 6, no. 3, pp. 311–335, Mar 1998. [Online]. Available: <https://doi.org/10.1023/A:1008889222784>
- [6] G. Matz, "On non-wssus wireless fading channels," *IEEE Transactions on Wireless Communications*, vol. 4, no. 5, pp. 2465–2478, Sep. 2005.
- [7] D. J. Thomson, "Spectrum estimation and harmonic analysis," vol. 70, no. 9, pp. 1055 – 1096, September 1982.
- [8] D. Slepian, "Prolate spheroidal wave functions, fourier analysis, and uncertainty — v: the discrete case," *The Bell System Technical Journal*, vol. 57, no. 5, p. Slepian78, May 1978.
- [9] L. Bernadó, T. Zemen, F. Tufvesson, A. F. Molisch, and C. F. Mecklenbräuker, "Delay and doppler spreads of nonstationary vehicular channels for safety-relevant scenarios," *IEEE Transactions on Vehicular Technology*, vol. 63, no. 1, pp. 82–93, Jan 2014.
- [10] N. Czink, "The random-cluster model – a stochastic mimo channel model for broadband wireless communication systems of the 3rd generation and beyond," Ph.D. dissertation, TU Wien, 2007.
- [11] A. F. Molisch, *Wireless Communications*. John Wiley & Sons, 2010.
- [12] M. Friese, "Multitone signals with low crest factor," *IEEE Transactions on Communications*, vol. 45, no. 10, pp. 1338–1344, Oct 1997.